electricity

MDPI

Article

Simple Chargers for a Small DC Micro-Grid for a Home Emergency Power System

Felix A. Himmelstoss * and Helmut L. Votzi

Faculty Electronic Engineering & Entrepreneurship, University of Applied Sciences Technikum Wien, 1200 Vienna, Austria

* Correspondence: felix.himmelstoss@technikum-wien.at

Abstract: Recently, the danger of a long blackout is discussed in Europe. Blackouts can be caused by failures in the energy distribution, errors in large power plants or even cyber-attacks. This can lead to a chain reaction and a disintegration of the mains. Longer blackouts have an extreme impact on the economy as a whole and on local households. Therefore, a small local grid at home which can supply the most important loads over some time has garnered increasing interest. With a small direct current (DC) grid, critical loads such as for deep freezers and refrigerators can be supplied, and some LED lights can be used in the evening or at night. Solar generators (panels) can be used to charge energy storage devices, e.g., batteries. A DC grid can not only be used in the case of an emergency, but can also be used to reduce energy consumption out of the public mains and reduce energy bills. The architecture of the household emergency DC grid is discussed; suggestions for batteries are given; two simple chargers, based on DC-DC-converters like the Buck (step-down) and on the Boost (step-up) converters, are shown; dimensioning suggestions are given; and simple, robust controllers, a P-controller with disturbance feedforward and a hysteresis controller, are treated and tested via simulations. The goal of the paper is to show a simple autonomous home energy system without an external fieldbus, LAN or internet connection with special focus on simple charger topologies.

Keywords: micro-grid; solar system; Buck converter; Boost converter; hysteresis control; disturbance feedforward

Citation: Himmelstoss, F.A.; Votzi, H.L. Simple Chargers for a Small DC Micro-Grid for a Home Emergency Power System. *Electricity* **2023**, *4*, 216–234. https://doi.org/10.3390/electricity4030013

Academic Editor: Kaisar R. Khan

Received: 30 March 2023
Revised: 10 June 2023
Accepted: 16 June 2023
Published: 26 June 2023

1. Introduction

Recently, the danger of a large blackout is often being discussed in the newspapers in Europe. Blackouts can be caused by failures in the energy distribution or by failures in large power plants. This can lead to a chain reaction and a disintegration of the mains. Additionally, extreme weather can lead to large disturbances in the mains. Longer blackouts have an extreme impact on the economy as a whole and on local households. Therefore, a small local grid at home which can supply the most important loads over some time has gained increasing interest. With a small DC grid, critical loads such as for deep freezers and refrigerators can be supplied, and some LED lights can be used in the evening or at night. Furthermore, laptops can be charged, which can enable some kind of home office to be made (without an internet connection). The energy for this micro-grid can be stored in batteries. If a car is available, the battery of it can also be connected. Solar generators (panels) can be used to charge the batteries. The use of an additional emergency grid in a private household is a new concept to supply important loads that has been suggested due to the risk of longer blackouts in the future. Up to now, such emergency systems have only been used in hospitals, some public buildings, data processing centers and critical infrastructure. For the last few decades, the risk of a blackout in the public mains has been very low in central Europe.

Energy costs have also increased very much. It should therefore be mentioned that this DC grid can not only be used in an emergency case but can also be used to reduce

energy consumption out of the public mains and reduce energy bills. In this paper, we present two simple charging topologies to supply a DC bus or to directly feed energy into a storage battery. We use simple controllers to avoid cyber-attacks in this emergency system. Cyber-attacks represent an important topic which is now often studied (e.g., [1–4]). Energy management for smart buildings has been discussed, e.g., in [5]. However, the aim of our system is as follows: the simpler the system, the higher the protection against outer attacks. The chargers treated here are as simple as possible.

Figure 1 shows the line diagram of the emergency DC micro grid. (1) symbolizes the solar generators. (2) represents a unidirectional DC/DC converter which feeds directly into the DC bus. (3) depicts a storage battery which is connected to a solar generator via a unidirectional DC/DC converter on one side (10) and is connected to a bidirectional DC/DC converter (4) to the DC bus on the other side. On the right side of the bus, a unidirectional DC/DC converter (5) is used to supply lighting devices (7, e.g., light-emitting diodes (LEDs)). With the DC/AC converter (6), a motor load (8), e.g., from a refrigerator, is supplied. This converter (6) can be uni- or bidirectional. The buffer of the DC bus is shown exemplary as a large capacitor (9), realized as a supercapacitor or a battery.

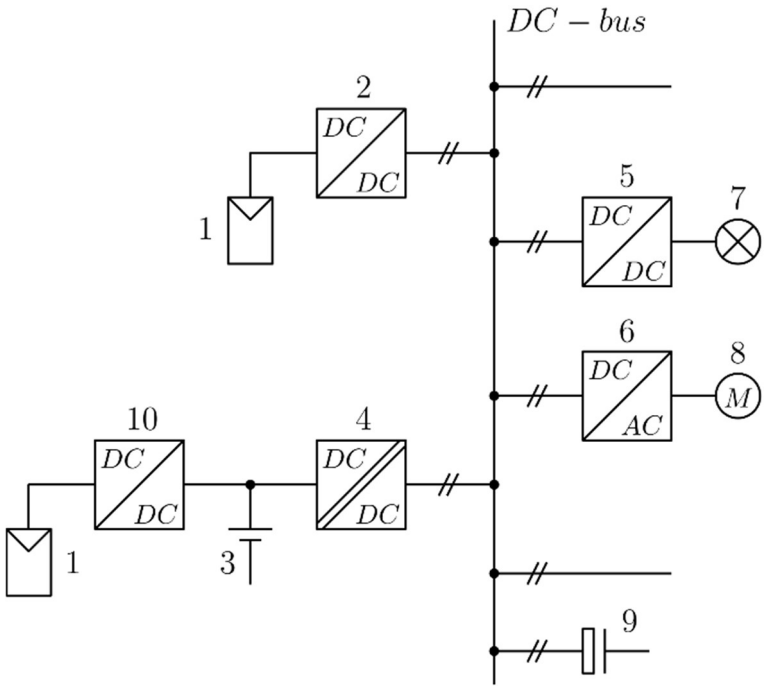

Figure 1. Topology of the DC emergency micro grid.

Only building blocks 2 and 10 are treated. Here, only unidirectional power flow is necessary. The converters can have step-up or step-down behavior, depending on the solar generator used. For the series connection of several panels, a step-down converter is used. Series connection has the advantage that a low current has to be handled. Small systems with low voltage need a step-up converter. The basics of power electronics and converter design can be found in textbooks.

Figure 2 shows the details of a system with only one solar generator (1) and one unidirectional DC/DC converter (2). With the switch, S, the converter can charge the battery (3) or directly charge the DC bus.

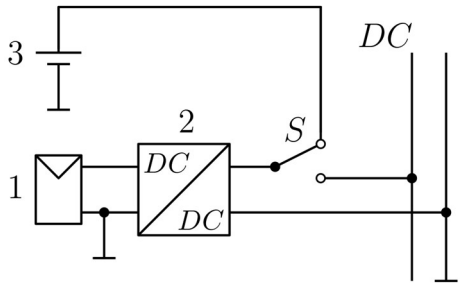

Figure 2. Details of a single solar generator system.

For DC micro-grids two system types are used, low voltage (LVDC) with, e.g., 48 V and high voltage (HVDC) with 380 V. For lower power loads the 48 V system is interesting for inter-house use, because typical distances are in a region of under 100 m where a 4 mm^2 cable is standard and sufficient. A low voltage is also advantageous for security reasons. For bigger systems with higher distances and loads, a 380 V system is the better choice [6].

Standard converters like Buck, Boost, SEPIC and Zeta are normally used for connecting different loads and sources. These could be solar panels, battery packs, or different household loads as shown in Figure 1 [6,7] Depending on the application, these converters are realized uni- or bidirectional as shown in Figure 1 [6,8].

The papers [7,9] show that lead–acid batteries are still used in battery storage units. The advantages are relatively low cost and the fact that four batteries in series provide a voltage of 48 V. In the papers [9,10] lithium-ion batteries are used as a storage unit. An advantage is the higher number of possible cycles and increased lifetime compared to lead–acid batteries. Additionally, the higher energy density in volume and weight can be seen as an advantage [9]. Another interesting fact is that LiFePo4 battery packs are available with a similar nominal voltage of 12.8 V as a lead—acid battery with 12 V. Classical lithium-ion battery packs are available with 14.4 V which fits not to form 48 V. Typical battery packs for smaller household applications could be formed by standard types with approximately 100 Ah [7,9].

Lead—acid batteries are still commonly used in storage units. Important parameters are the inner resistance and the discharge current. The inner DC resistance can be used for, e.g., the estimation of the voltage drop under load conditions. For a 100 Ah lead–acid battery the internal resistance can have a value of approximately 4.5 mΩ and a maximal discharge current of 800 A (for 5 s) is possible [11].

For considering the dynamic behavior Randles circuit can be used as battery model which is explained with typical parameters in [12]. Different examples for AC impedance plots and parameters of different batteries are shown and explained in [13–15].

Basics of power electronics and converter design can be found in the textbooks, e.g., [16–18]. A single-phase grid interface for home energy storage is described in [19]. Ref. [20] shows relatively complex converter topologies for charging electric vehicles (EVs) and compare them with a bidirectional step-up-down converter. In [21] the benefits of a DC home grid are shown and typical private household consumer power loads are listed. Ref. [22] gives an overview of single-stage isolated AC-DC topologies for interfacing DC and AC grids, and building up on this, in [23] the hold-up time is treated. Ref. [24] shows a multi output converter which can be used for an off-grid DC system. The parameters used in the study, which are typical for such a system, are also given. Charging an EV from a home DC grid is treated in [25].

In [26] interesting standards for DC grids and the requirements for different loads are listed, whereas the focus lays on the DC distribution technology. DC transformer topologies are compared. Similarities and differences of protection devices between AC and DC systems are treated. A performance analysis of a Boost converter structure in a photo voltaic (PV) system with maximum power point (MPP) tracking which supplies a DC grid is shown in [27]. Voltage standards of DC residential power systems are compared

in [28]. Integrating a PV and a small hydrogen power source into a charging infrastructure is shown in [29].

2. Buck Battery Charger

Figure 3 shows the circuit diagram of the battery charger (or a device to feed directly into the DC bus) derived from the Buck converter. The output is formed by the battery so the output voltage is constant. The converter must therefore be current-controlled. Nevertheless, a capacitor between the output connectors (3, 4) of the converter is used to avoid that the high frequency component of the current flows through the battery and there produces additional heat. The input capacitor between the input connectors (1, 2) is used to compensate for the inductance of the wires between the solar generator and the converter. Furthermore, the pulsed input current does not burden the solar generator. The diode D_2 must be somewhere between the input and the output to avoid a current out of the battery when the input voltage is lower than the output voltage. The body diode of the MOSFET would discharge the battery, feed energy back into the solar generator and could even destroy it. This diode is better placed at the input, where the current is lower because the converter has a step-down topology and therefore the mean current is lower at the input side than at the output (input and output power are equal), or the diode is already included in the solar generator. For continuous input current it is useful (if the inductance of the cables used to connect the converter is small), to connect a coil between input connector (1) and the anode of the diode D_2.

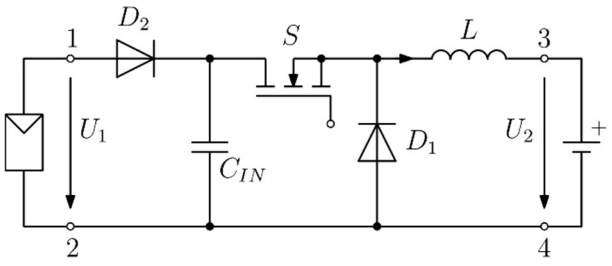

Figure 3. Buck battery charger for a solar generator (input inductance and capacitor in parallel to the battery are not shown, see text).

The easiest way to control this converter is by a hysteresis controller. For the description we used ideal components. When the active switch S is turned on, the difference between the input (the voltage across C_{IN}) and the output voltages is across the inductor and the current increases. When the current reaches the upper limit, the controller turns the switch off, and when the current reaches the lower limit, the controller turns it on again. The difference between the upper- and the lower current limits, the hysteresis, is written by ΔI. The on-time of the switch is therefore

$$U_1 - U_2 = L\frac{\Delta I}{T_{on}} T_{on} = L\frac{\Delta I}{U_1 - U_2} \tag{1}$$

During the off-time, the negative output voltage reduces the current by ΔI during the time

$$T_{off} = L\frac{\Delta I}{U_2}. \tag{2}$$

The switching period is now the sum of the on- and off-times

$$T = L\frac{\Delta I}{U_1 - U_2} + L\frac{\Delta I}{U_2} = L\Delta I\frac{U_1}{U_2(U_1 - U_2)} \tag{3}$$

or more usually given as switching frequency

$$f = \frac{1}{L\Delta I}\frac{U_2(U_1 - U_2)}{U_1}. \tag{4}$$

Changes of the input and output voltages change only the frequency. This controller concept is very robust. One can also notice that the lower the voltage ripple, the higher the occurring frequency. A low current ripple increases the frequency but decreases the bypass capacitor for the battery.

2.1. Dimensioning

During the off-time of the active switch, the inductor voltage equals the negative output voltage. When a maximum switching frequency is chosen, the inductor value can be calculated from (4) according to:

$$L = \frac{1}{f\Delta I}\frac{U_2(U_1 - U_2)}{U_1}. \tag{5}$$

When the input voltage is minimal and the output voltage is maximal, the on-time has a maximum, and when the input voltage has a maximum and the output voltage has its minimum, the on-time is minimal. During the off-time no current is taken from the source. To get a continuous current out of the solar generator, an additional inductor should be placed between the input capacitor and the solar generator.

Figure 4 shows the simulation model implemented by LTSpice of a Buck battery charger with hysteresis controller. The current is measured with the voltage source V3 and transferred into the actual value for the controller by the current controlled voltage source H1. The reference value is generated by the voltage source V4. The hysteresis controller is realized by the comparator U1, and the hysteresis is fixed by the resistors R1 and R2 which form the positive feedback. The voltage-controlled voltage source E1 is used to form an isolated driver. The factor 10 increases the signal from the and-gate A1, which combines the output signal of the comparator with a start signal. The comparator has to be supplied by plus/minus 5 V. It should be mentioned here that one can also use a single supplied comparator.

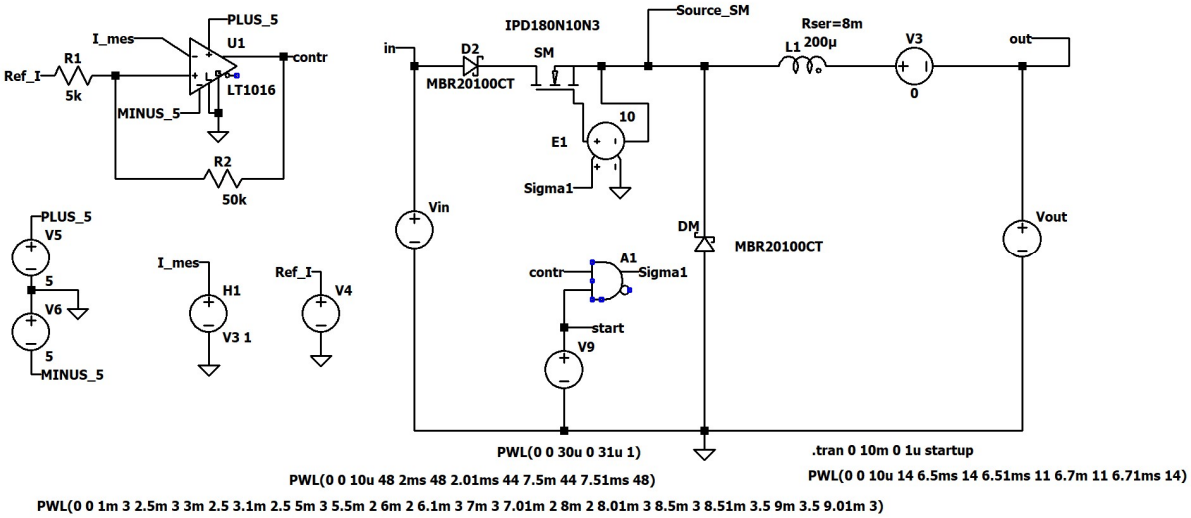

Figure 4. Buck converter with hysteresis controller.

Figure 5 shows the input voltage, the reference value, and the current through the inductor which is equal to the charging current. The output current ensues from the reference value. Steps in the input voltage are corrected immediately.

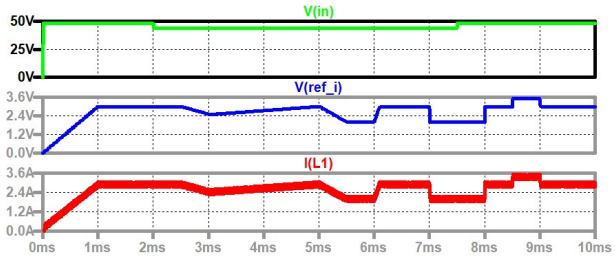

Figure 5. Hysteresis-controlled Buck converter (up to down): input voltage (green), reference value (blue), current through the coil (charging current, red).

When a small inductor is connected in series to the solar generator, one can measure a nearly constant current, which can be used for the maximum power point (MPP) tracker. The MPP power $I_{MMP} \cdot U_{MPP}$ must be equal to the output power $U_2 \cdot I_L$. With an approximated efficiency of

$$\eta = \frac{U_2 I_L}{U_{MPP} I_{MPP}} \tag{6}$$

one can calculate the reference value for the controller

$$I_{L,ref} = \frac{\eta U_{MPP} I_{MPP}}{U_2}. \tag{7}$$

2.2. Model of the Buck Battery Charger

To design a linear controller, the model of the battery charger has to be derived. The battery voltage changes very slowly. So, one can set the output voltage to a constant value U_2. The output voltage of the solar generator can change quickly, but the input capacitor reduces the derivative of the voltage at the input u_1. The derivative of the inductor current during mode M1 (active switch S on and passive switch D_1 off) can therefore be written according to

$$\frac{di_L}{dt} = \frac{u_1 - U_2}{L}. \tag{8}$$

In mode M2 (active switch S off and passive switch D_1 on) one can write

$$\frac{di_L}{dt} = \frac{-U_2}{L}. \tag{9}$$

Using a fixed frequency and a duty cycle d, one can combine the two equations (using the state-space averaging method) according to

$$\frac{di_L}{dt} = \frac{u_1 \cdot d - U_2}{L}. \tag{10}$$

Inserting the perturbation approach leads to

$$\frac{d\hat{i}_L}{dt} = \frac{\left(U_1 + \hat{u}_1\right)\left(D_0 + \hat{d}\right) - U_2}{L}. \tag{11}$$

The differential equation for the perturbation around the operating point is now

$$\frac{d\hat{i}_L}{dt} = \frac{D_0 \hat{u}_1 + U_1 \hat{d}}{L}. \tag{12}$$

The connection between input and output voltages at the operating point can be found from

$$-U_2 + D_0 U_1 = 0. \tag{13}$$

This leads to the well-known equation

$$U_2 = U_1 D_0. \tag{14}$$

Figure 6 shows the signal flow graph of the charger with the controller K_R. I_L*(s) describes the desired value and I_L(s) the actual value. Signal flow graphs are a very useful tool to describe systems in a graphical way. In [30] a short summary of the elements and the construction of signal flow graphs is explained, and with the use of Mason's equation the transfer function of a system can be calculated.

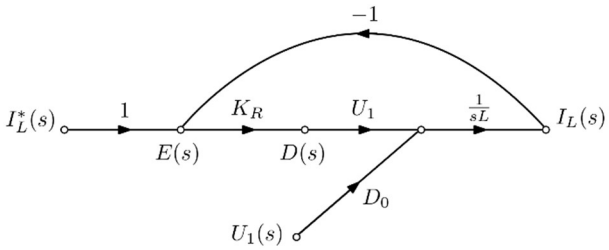

Figure 6. Signal flow graph of the controlled Buck-derived charger.

The output value is the current through the coil, which is also the charging current (the mean value flows through the battery and the ripple flows through the capacitor which is in parallel to the battery). First, we studied the transfer function between the load current and the duty cycle and the transfer function between the load current and the input voltage. The signal flow graph of the converter can now be drawn (Figure 6).

The transfer function between the inductor current and the duty cycle

$$G_{ID}(s) = \frac{I_L(s)}{D(s)} = \frac{U_1}{sL} \tag{15}$$

shows an integral behavior which is depicted in Figure 7.

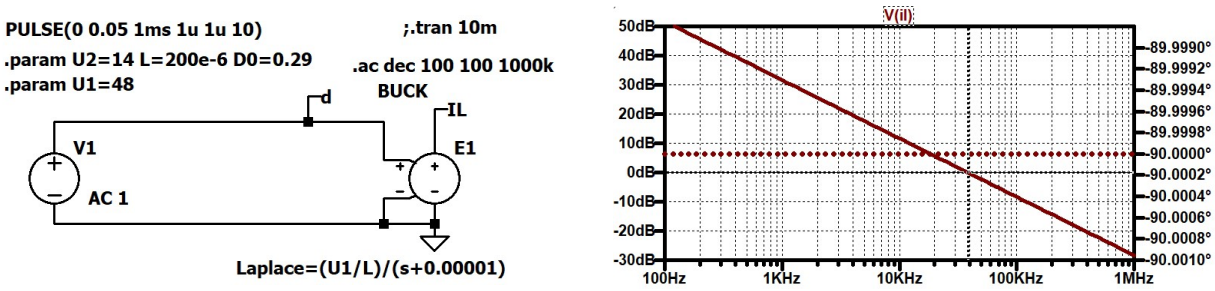

Figure 7. Buck-derived battery charger, duty cycle to charging current transfer function: simulation circuit, Bode plot (solid line: gain response, dotted line: phase response).

The transfer function between the current through the inductor and the input voltage

$$G_{IU}(s) = \frac{I_L(s)}{U_1(s)} = \frac{D_0}{sL} \tag{16}$$

also shows an integral behavior (Figure 8).

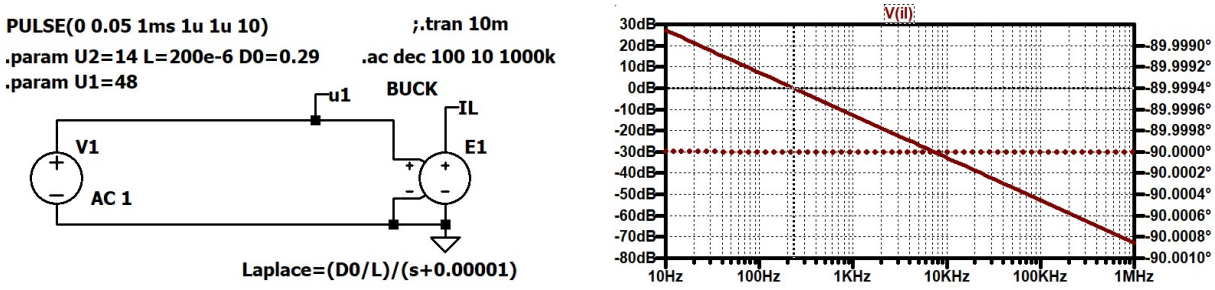

Figure 8. Buck-derived battery charger, disturbance (input voltage) to output (charging current) transfer function: simulation circuit, Bode plot (solid line: gain response, dotted line: phase response).

Using a P-controller one obtains the control transfer function according to Figure 6

$$G_{IIref}(s) = \frac{I_L(s)}{I_{ref}(s)} = \frac{\frac{K_R U_1}{sL}}{1 + \frac{K_R U_1}{sL}} = \frac{K_R U_1}{sL + K_R U_1} = \frac{1}{s\frac{L}{K_R U_1} + 1} \tag{17}$$

and for the disturbance transfer function according to Figure 6

$$G_{IUclosed}(s) = \frac{I_L(s)}{U_1(s)} = \frac{\frac{D_0}{sL}}{1 + \frac{K_R U_1}{sL}} = \frac{D_0}{sL + K_R U_1} = \frac{D_0}{K_R U_1} \frac{1}{s\frac{L}{K_R U_1} + 1}. \tag{18}$$

From the control transfer function one can see that no steady error occurs, but from the disturbance transfer function one can see that an error will occur. When the input voltage changes by ΔU_1, the error can be calculated according to

$$\Delta I_L = \frac{D_0}{K_R U_1} \Delta U_1. \tag{19}$$

For a low error, a high input voltage and a large controller gain is helpful. Figure 9 shows the simulation circuit and the Bode plot for the open loop with a P-controller. The transfer function between output current and duty cycle is calculated by the voltage-controlled voltage source E1, the source E2 is used to model the controller. In the simulation model the pole of the plant is a little bit shifted to the left. This is necessary when a transient analysis is performed to avoid a singular calculation matrix.

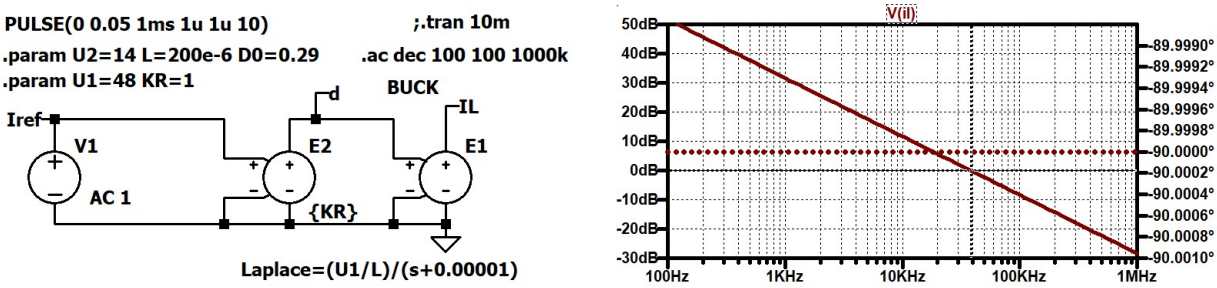

Figure 9. Buck-derived battery charger open loop with P-controller with $K_R = 1$: simulation circuit, Bode plot (solid line: gain response, dotted line: phase response).

Figure 10 shows the closed loop system. The error between the reference value and the actual value is calculated by the arbitrary voltage source B1. As expected, the closed loop shows a PT1 behavior.

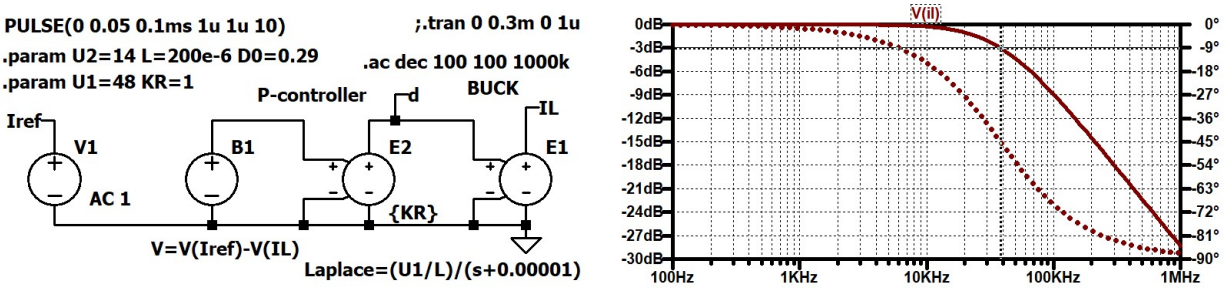

Figure 10. Buck-derived battery charger, closed loop with P-controller: simulation circuit, Bode plot (solid line: gain response, dotted line: phase response).

Figure 11 shows the step response of two different controller gains ($K_R = 1$, $K_R = 0.2$). With $K_R = 1$ the corner frequency is about 40 kHz (Figure 10), and with the second value ($K_R = 0.2$) one gets a corner frequency of the closed loop system of 7.5 kHz.

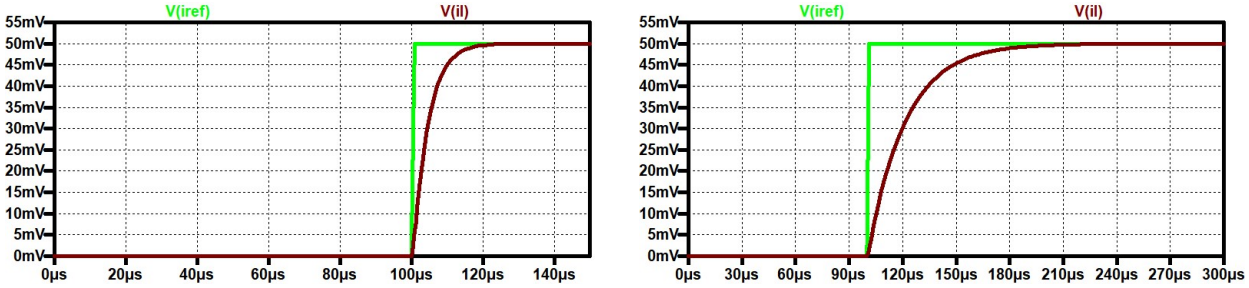

Figure 11. Buck-derived battery charger, closed loop with P-controller, step response: $K_R = 1$ and $K_R = 0.2$.

Figure 12 shows the influence of a reference value step and of an input voltage step. The reference value step does not lead to a steady-state error, but the voltage step leads to one.

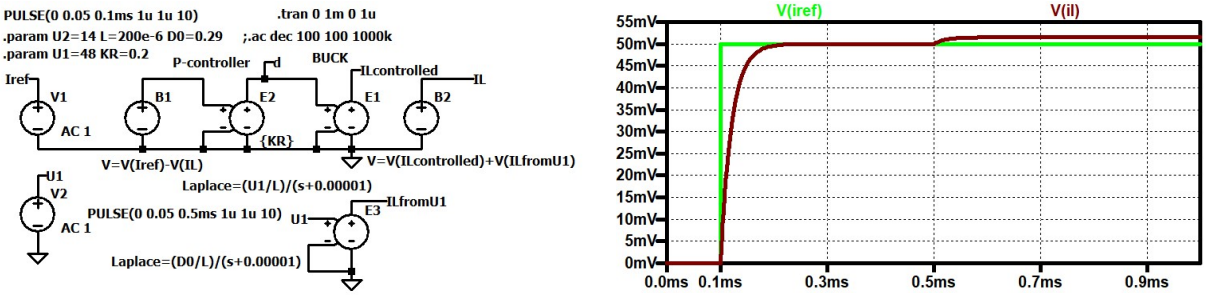

Figure 12. Buck-derived battery charger, closed loop with P-controller $K_R = 0.2$, influence of input voltage change: simulation circuit, step response.

From the disturbance transfer function one can calculate the disturbance *Dist* according to $Dist = \frac{D_0}{K_R U_1} \Delta U_1 = \frac{0.29}{0.2 \cdot 48\ \mathrm{V}} 0.05\ \mathrm{V} = 1.5\ \mathrm{mA}$, represented by 1.5 mV in the simulation. That means that the error is 1.5 mA. Please keep in mind that in our simulation currents are represented by voltages.

The error is only 3%. A change in ΔU_1 of 1 V would result in an error of 30.2 mA (or an error of 60%)!

The integrating plant also integrates the disturbance and therefore a steady state error occurs caused by the input voltage!

The easiest way to reduce the error is to use a disturbance feedforward. This is performed by including an edge with the value $-K(s)$ between the disturbance $U_1(s)$ and

the input of the converter $D(s)$ into the signal graph (Figure 13). I_L*(s) describes the desired value and I_L(s) the actual value. The output $I_L(s)$ is therefore influenced by the input voltage in two ways: directly by the disturbance connection $G_{IU}(s)$ (16) and by the new path $-K{\cdot}G_{ID}(s)$, with G_{ID} from (15).

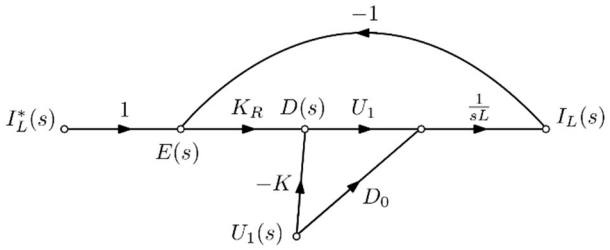

Figure 13. Signal flow graph of the controlled Buck-derived charger with disturbance feedforward.

The current change at the output caused by the input voltage change is therefore

$$I_L(s) = [G_{IU}(s) - K(s){\cdot}G_{ID}]{\cdot}U_1(s). \tag{20}$$

To compensate for the influence of changes at the input voltage, the terms within the rectangular brackets must be zero. The compensator K can be calculated according to

$$K(s) = \frac{G_{IU}(s)}{G_{ID}(s)} = \frac{D_0}{U_1}. \tag{21}$$

The compensation is more efficient when the input voltage is high. Figure 14 shows the simulation circuit and the response of the output current concerning a reference value step and step changes of the input voltage. The disturbance feedforward compensates for the influence of the changes of the input voltage. The compensator is included in the arbitrary voltage source B3.

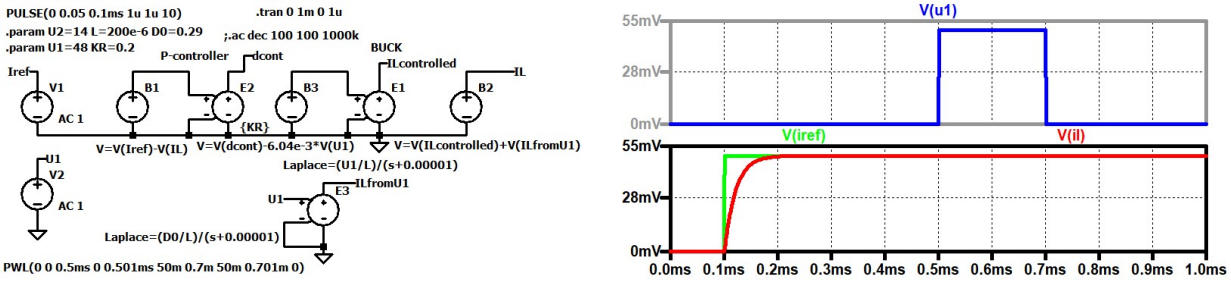

Figure 14. Buck-derived charger with disturbance feedforward: simulation circuit and step responses.

Summarizing, one can say that the P-controller should be extended by a disturbance feedforward, to avoid a pronounced error caused by input voltage changes.

3. Simple Boost Battery Charger

When the solar generator output voltage is lower than the voltage of the storage device, a step-up converter has to be used. Figure 15 shows the circuit diagram. The coil L_O smoothes the output current. Parallel to the output connectors (3, 4) a small capacitor (not drawn) can be mounted. Parallel to the input connectors (1, 2) a capacitor C_{IN} is connected.

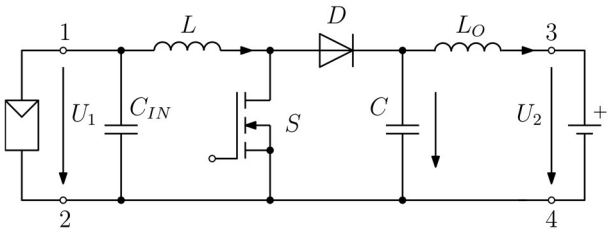

Figure 15. Boost converter battery charger.

When the active switch is on, the input voltage is across the inductor and the current rises. When the current reaches the upper limit, the active switch is turned off and the current decreases, because the difference between the input and the output voltages, which is negative, lies across the inductor. When the lower current limit is reached, switch S is turned on again. With the difference between the upper and the lower limit ΔI, the on and off times can be calculated according to

$$T_{on} = L\frac{\Delta I}{U_1} \tag{22}$$

$$T_{off} = L\frac{\Delta I}{U_2 - U_1}. \tag{23}$$

This leads to the switching period

$$T = L\frac{\Delta I}{U_2} + L\frac{\Delta I}{U_2 - U_1} = L\Delta I\frac{2U_2 - U_1}{U_2(U_2 - U_1)} \tag{24}$$

and to the switching frequency

$$f = \frac{1}{L\Delta I}\frac{U_2(U_2 - U_1)}{2U_2 - U_1}. \tag{25}$$

3.1. Determination of the Desired Current Value

To optimize the charging, the desired current value should be near to the maximum power point value. This value has to be found with a maximum power point (MPP) tracker. The charging current I_{LOAD} is connected to the MPP current I_{MMP} by the charge balance of the capacitor C

$$I_{LOAD}T_{on} = (I_{MPP} - I_{LOAD})T_{off}. \tag{26}$$

Toff is the difference between the switching period and the on-time of the active switch. Inserting (22) and (23) leads to

$$I_{LOAD}L\frac{\Delta I}{U_1} = (I_{MPP} - I_{LOAD})L\frac{\Delta I}{U_2 - U_1}. \tag{27}$$

The charging current is dependent on the MPP-current and the input voltage (which is the resulting MPP value) and the constant output voltage according to

$$I_{LOAD} = I_{MPP}\frac{U_1}{U_2}. \tag{28}$$

This result is correct, because in the ideal case the input power and the output power must be equal.

3.2. Design of the Inductor

The shortest on-time occurs when the voltage is at its maximum (we take the maximum at the MPP). When one fixes the minimum on-time to $T_{on\min}$ and fixes the maximum current ripple, one gets the value of the coil according to

$$L = \frac{U_{1\max} T_{on\min}}{\Delta I}. \tag{29}$$

The current at the input has the same current ripple. This ripple current produces a voltage ripple across the input capacitor which is the sum of the voltage across the (ideal) C_{IN} and the voltage drop across the series resistor of the capacitor R_{CIN}.

$$\Delta u_{CIN} = \frac{1}{C_{IN}} \frac{T}{2} \frac{\Delta I}{2} + R_{CIN} \Delta I. \tag{30}$$

Inserting the switching period (24) one gets

$$C_{IN} = \frac{1}{4(\Delta u_{CIN} - R_{CIN} \Delta I)} L (\Delta I)^2 \frac{2U_2 - U_1}{U_2 (U_2 - U_1)}. \tag{31}$$

The output capacitor which is in parallel to the load forms a short-circuit for the pulse frequency. The load cannot be directly connected to the output connectors (3, 4), but connected via cables. If needed, one can improve the converter (reducing the current ripple) by an additional inductor L_2.

During the on-time of the active switch no energy is transferred from the input side to the output side. The mean current through the second inductor is equal to the load current which charges the battery. This current discharges the capacitor *C*. At the lowest input voltage, the on-time has its maximum.

The voltage across *C* decreases by the value

$$\Delta u_C = \frac{1}{C} \int_0^{Ton,\max} I_{Load} dt. \tag{32}$$

The capacitor must therefore be larger than

$$C = \frac{1}{\Delta u_C} I_{Load} L \frac{\Delta I}{U_{1\min}}. \tag{33}$$

3.3. Dynamics

The battery voltage is changing very slowly. So, one can consider the output voltage U_2 constant. The change in the inductor current during mode M1 can therefore be written according to

$$\frac{di_L}{dt} = \frac{u_1}{L}. \tag{34}$$

In mode M2 one can write

$$\frac{di_L}{dt} = \frac{u_1 - U_2}{L}. \tag{35}$$

Using a fixed frequency and the duty cycle d, one can combine the two equations according to

$$\frac{di_L}{dt} = \frac{u_1 - U_2(1-d)}{L}. \tag{36}$$

Inserting the perturbation ansatz leads to

$$\frac{d\hat{i}_L}{dt} = \frac{U_1 + \hat{u}_1 - U_2 + U_2\left(D_0 + \hat{d}\right)}{L}. \tag{37}$$

The differential equation for the perturbation around the operating point is now

$$\frac{d\hat{i}_L}{dt} = \frac{\hat{u}_1 + U_2\hat{d}}{L}. \tag{38}$$

The connection of the operating point values can be found from

$$U_1 - U_2 + D_0 U_2 = 0. \tag{39}$$

This leads to the well-known equation

$$U_2 = \frac{U_1}{1 - D_0}. \tag{40}$$

The signal flow graph of the converter can now be drawn (Figure 16), I_L*(s) again describes the desired value and $I_L(s)$ the actual value.

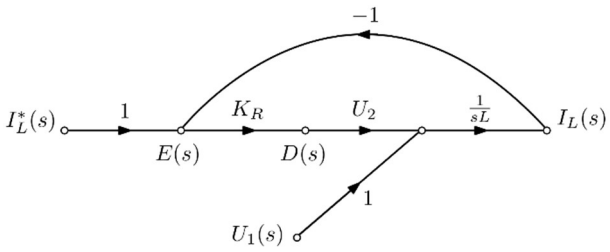

Figure 16. Signal flow graph of the controlled Boost charger.

The transfer function between the inductor current and the duty cycle (Figure 17) is

$$G_{ID}(s) = \frac{I_L(s)}{D(s)} = \frac{U_2}{sL}. \tag{41}$$

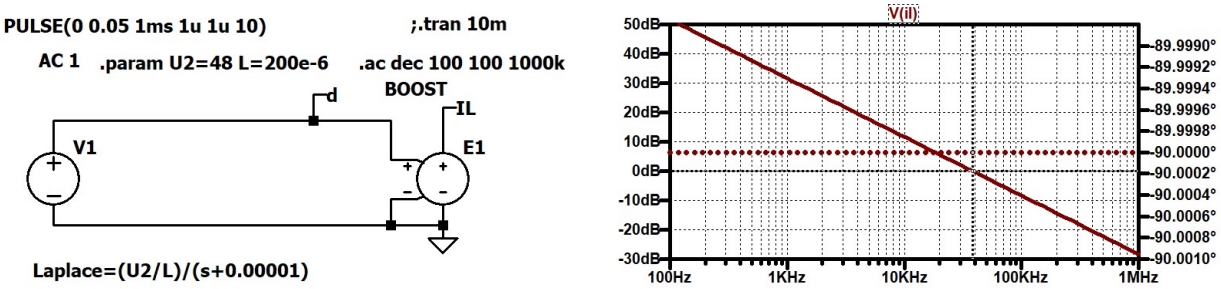

Figure 17. Boost battery charger, output to input transfer function: simulation circuit, Bode plot (solid line: gain response, dotted line: phase response).

The transfer function between the current through the inductor and the input voltage (Figure 18) is

$$G_{IU}(s) = \frac{I_L(s)}{U_1(s)} = \frac{1}{sL}. \tag{42}$$

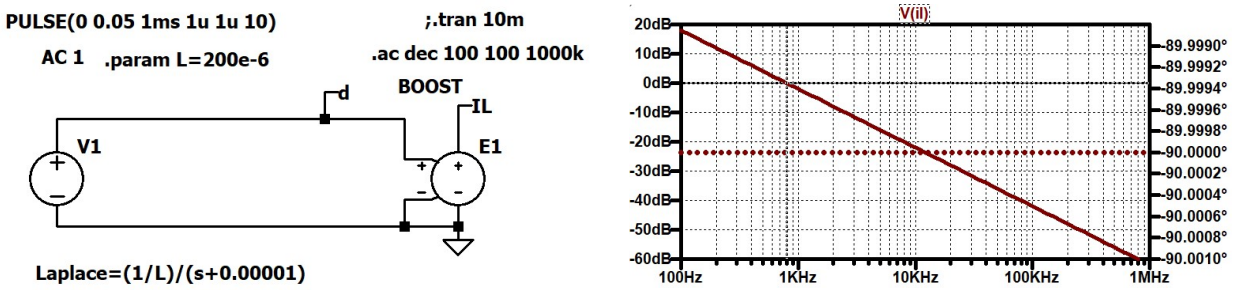

Figure 18. Boost battery charger, disturbance to output transfer function: simulation circuit, Bode plot (solid line: gain response, dotted line: phase response).

The plant has an integral behavior so a P-controller can be used. The control transfer function according to Figure 16 can be calculated to

$$G_{IIref}(s) = \frac{I_L(s)}{I_{ref}(s)} = \frac{\frac{K_R U_2}{sL}}{1 + \frac{K_R U_2}{sL}} = \frac{K_R U_2}{sL + K_R U_2} = \frac{1}{s\frac{L}{K_R U_2} + 1}. \tag{43}$$

The disturbance transfer function according to Figure 16 results in

$$G_{IUclosed}(s) = \frac{I_L(s)}{U_1(s)} = \frac{\frac{U_2}{sL}}{1 + \frac{K_R U_2}{sL}} = \frac{U_2}{sL + K_R U_2} = \frac{1}{K_R}\frac{1}{s\frac{L}{K_R U_2} + 1}. \tag{44}$$

3.4. P-Controller

From the signal flow graph (Figure 16) and from the control transfer function one can see that a P-controller is sufficient to control the charger.

Figure 19 shows the open loop transfer function of the boost converter with a controller gain of $K_R = 1$. The open loop shows integral behavior, a line which is falling with -20 dB/decade.

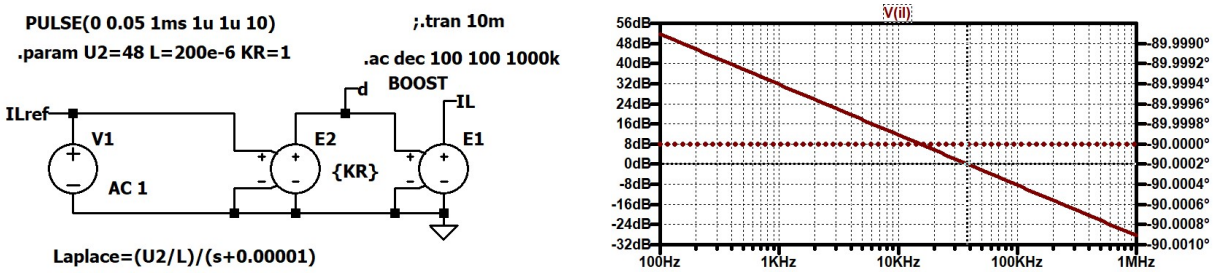

Figure 19. Open loop transfer function of the Boost converter, controller gain $K_R = 1$: simulation, Bode plot (solid line: gain response, dotted line: phase response).

The closed loop Bode diagram is shown in Figure 20 with $K_R = 1$. As expected, a PT1 behavior occurs.

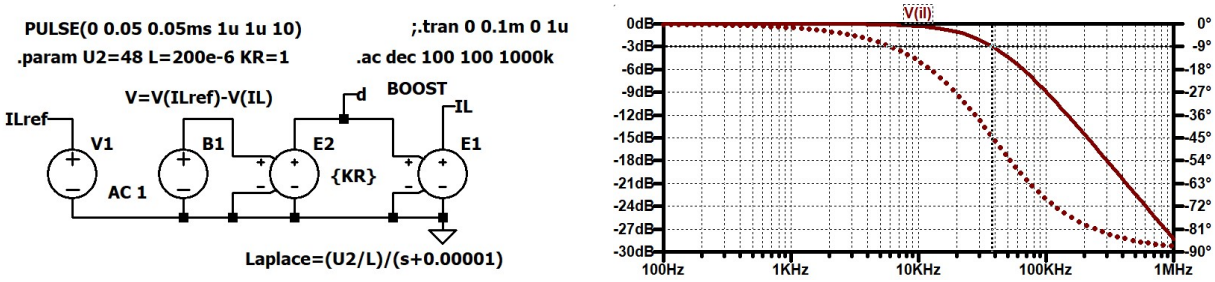

Figure 20. Closed loop transfer function of the Boost converter, controller gain $K_R = 1$: simulation, Bode plot (solid line: gain response, dotted line: phase response).

One has to keep in mind that the time constant of the controlled system should be larger than the switching period of the converter. The controller gain should therefore be reduced. Figure 21 shows the step response for $K_R = 1$ and for $K_R = 0.1$. The time constant is longer in the second case. In both cases there is no overshot, no ringing, and no stationary error.

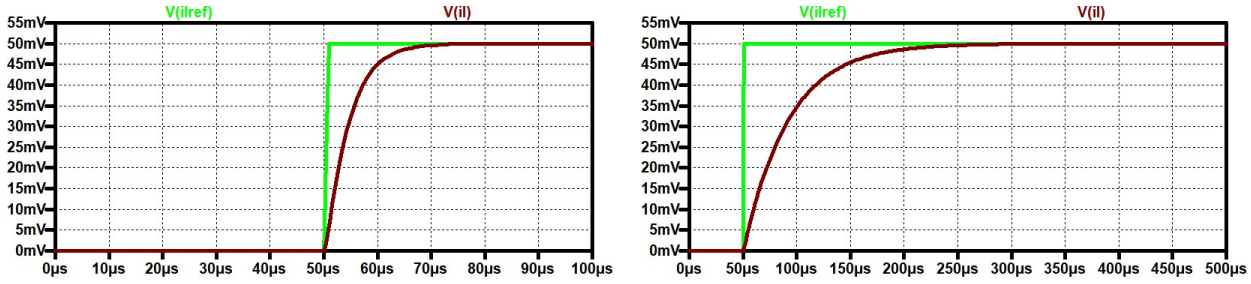

Figure 21. P controlled Boost converter step response: $K_R = 1$, $K_R = 0.2$.

Here, we studied the influence of the input voltage. From the disturbance transfer function (44) one can recognize that a steady state error will occur. Figure 22 shows the influence of the change in the input voltage. A change in the reference value leads to no error, but a change in the input voltage leads to an error of the current. The smaller the controller gain, the larger is the current error.

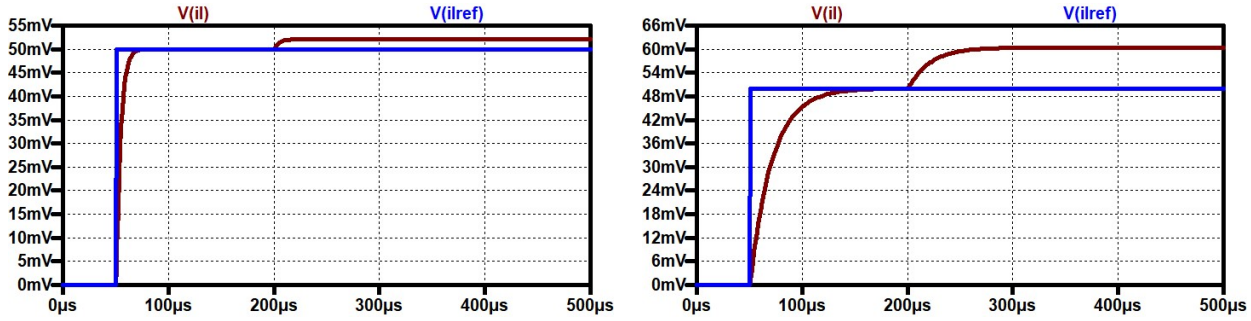

Figure 22. P controlled Boost converter, reference value and input voltage step, step response: $K_R = 1$, $K_R = 0.2$.

The easiest way to improve the behavior is to use a disturbance feedforward to reduce the error. As shown in (21) the feedforward compensator can be calculated by dividing the influence of the disturbance by the transfer function of the plant to be controlled. So, one writes for the compensator

$$K = \frac{\frac{1}{sL}}{\frac{U_2}{sL}} = \frac{1}{U_2}. \tag{45}$$

The higher the output voltage, the better will be the compensation. Figure 23 shows the simulation circuit for the disturbance feedforward and the reaction to a reference value step (0.5 A) and two steps of the input voltage (1 V). No error occurs now.

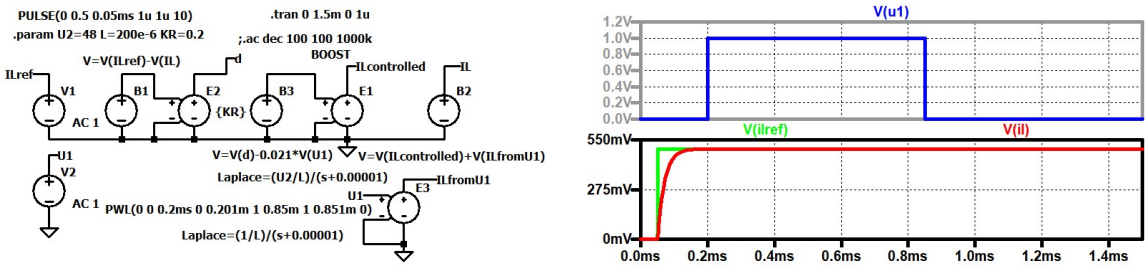

Figure 23. Boost charger with disturbance feedforward: simulation circuit and step responses.

Figure 24 shows a circuit-oriented simulation with a P-controller. The controller is realized by the OPA (operational amplifier) U2, the PWM modulator by the comparator U1. The current through the inductor is measured with the help of V3 and H1. The output signal of H1 can be filtered or better sampled in the middle of the on-time to obtain the mean value of the current. Figure 25 shows the input voltage, the reference value, and the current through the coil. A good match between the reference and the actual values can be achieved. The switching frequency is 100 kHz and is determined by the signal triangle.

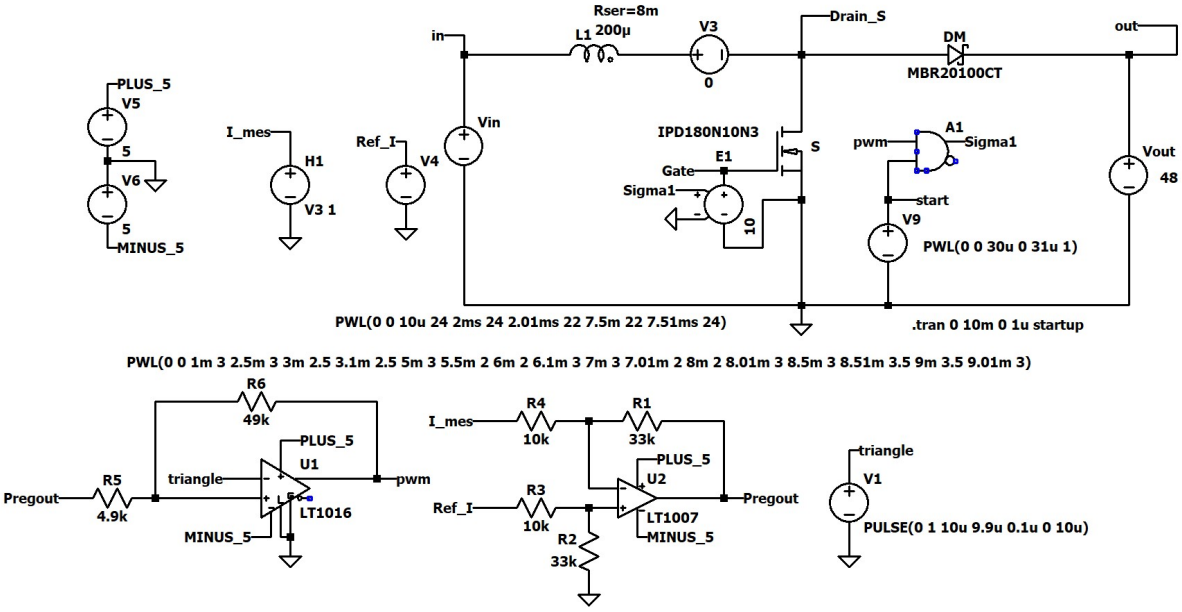

Figure 24. Circuit orientated simulation of the P-controlled Boost battery charger.

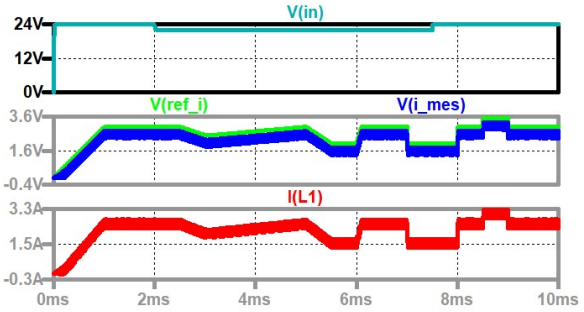

Figure 25. Circuit orientated simulation of the P-controlled Boost battery charger: input voltage (turquoise), reference value (green), current measurement signal (blue), current through the coil (red).

3.5. Hysteresis Controller

Figure 26 shows the simulation circuit of the hysteresis-controlled Boost converter. The current is measured by the voltage source V3 and transferred into the measurement signal I_mes. The controller is realized by the comparator U1 which has to be supplied with plus/minus 5 V. The width of the hysteresis is fixed by the resistors R1 and R2. The reference current is produced by the voltage source V4. With the piecewise linear voltage source V9, a start signal is generated. With this signal one can achieve that the clocking of the transistor starts after a possible inrush current when the system starts. In the depicted case the output voltage is higher than the input voltage; therefore, no inrush current occurs. The voltage-controlled voltage source E1 simulates the driver (the factor 10 multiplies the output of the AND-gate A1 by the factor ten to generate a sufficient gate signal for the MOSFET).

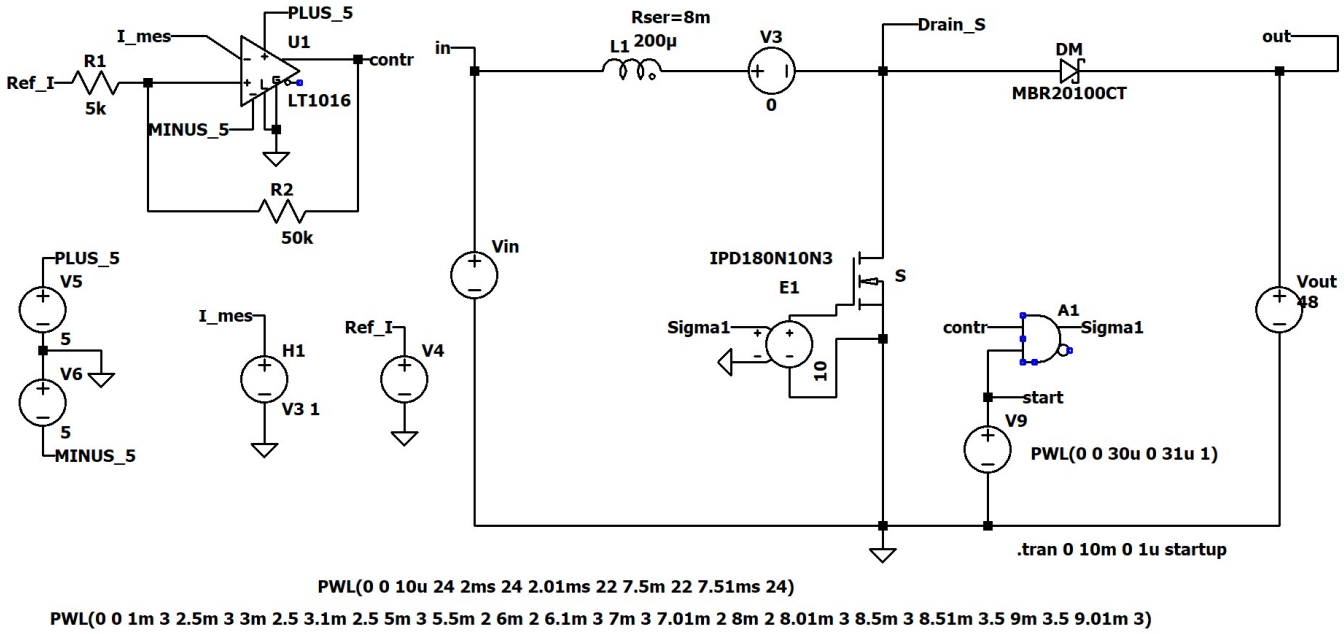

Figure 26. Boost converter with hysteresis controller.

The hysteresis controller leads to a very robust system. Figure 27 shows the behavior of the system. Steps of the input voltage have no influence on the current. Changes (ramps of the reference value or reference value steps) lead to an immediate reaction of the current. No overshot or ringing occurs.

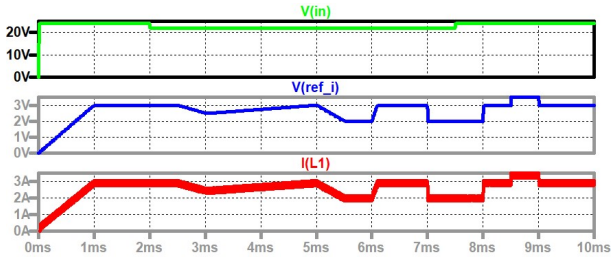

Figure 27. Hysteresis-controlled Boost converter (up to down): input voltage (green), reference value (1 V equals a desired current of 1 A, blue), current through inductor (red).

4. Conclusions

The potential damage of long blackouts for the economy and for the households is obvious. Therefore, it seems useful to integrate a small independent emergency DC-grid into private houses to fill the gap when the public mains are disrupted. Simple batteries

can be used as storage devices. The storage capacity depends on the loads which have to be supplied. The chargers described here have a simple topology and are derived from the DC-DC Buck and Boost converters. Due to the constant output voltage, the chargers can be described as first order systems with integral behavior. Therefore, P-controllers can be used. The disturbance transfer functions show, however, that a steady-state error will occur when the input voltage changes. The disturbance feedforward method can be used to improve the system. Another controller concept is the hysteresis controller. This concept is very robust concerning parameters and input value changes and corrects the actual value immediately. The effort for realizing such a home emergency DC-grid is low and the controllers for the chargers are resilient and easy to implement. Additionally, the system is immune to cyber-attacks. The storage capacity of this additional DC-grid can be used in accordance with a DC-AC converter to supply the AC mains of the household with the excess energy (e.g., from the solar generators when the storage devices are fully charged) to reduce the energy costs.

Author Contributions: Conceptualization, F.A.H.; writing, F.A.H.; simulation, F.A.H.; validation, F.A.H., H.L.V.; writing—original draft preparation, H.L.V.; writing—review and editing, H.L.V.; visualization, H.L.V. All authors have read and agreed to the published version of the manuscript.

Funding: This research received no external funding.

Data Availability Statement: Not applicable.

Acknowledgments: Open Access Funding by the University of Applied Sciences Technikum Wien.

Conflicts of Interest: The authors declare no conflict of interest.

References

1. Cecilia, A.; Sahoo, S.; Dragicevic, T.; Costa-Castello, R.; Blaabjerg, F. On Addressing the Security and Stability Issues Due to False Data Injection Attacks in DC Microgrids—An Adaptive Observer Approach. *IEEE Trans. Power Electron.* **2021**, *37*, 2801–2814. [CrossRef]
2. Burgos-Mellado, C.; Donoso, F.; Dragicevic, T.; Cardenas-Dobson, R.; Wheeler, P.; Clare, J.C.; Watson, A.J. Cyber-Attacks in Modular Multilevel Converters. *IEEE Trans. Power Electron.* **2022**, *37*, 8488–8501. [CrossRef]
3. Zhang, J.; Guo, L.; Ye, J. Cyber-attack Detection for Photovoltaic Farms based on Power-Electronics-Enabled Harmonic State Space Modeling. *IEEE Trans. Smart Grid* **2022**, *13*, 3929–3942. [CrossRef]
4. Qiu, W.; Sun, K.; Li, K.-J.; Li, Y.; Duan, J.; Zhu, K. Cyber-Attack Detection: Modeling and Roof-PV Generation System Defending. *IEEE Trans. Ind. Appl.* **2023**, *59*, 160–168. [CrossRef]
5. Chatterjee, A.; Paul, S.; Ganguly, B. Multi-Objective Energy Management of a Smart Home in Real Time Environment. *IEEE Trans. Ind. Appl.* **2023**, *59*, 138–147. [CrossRef]
6. Anees, M.; Moaz, T.; Hussain, S.; Khan, H.A.; Nasir, M. Evaluation of System Losses for 48V and 380V Solar Powered LVDC Microgrids. In Proceedings of the 2020 IEEE Power & Energy Society General Meeting (PESGM), Montreal, QC, Canada, 2–6 August 2020; pp. 1–5. [CrossRef]
7. Ambriz, O.; Onofre, L.; Hamlin, J.; Taufik, T.; Hasanah, R.N. Bi-Directional DC-DC Converter for the DC House Project. In Proceedings of the 2020 FORTEI-International Conference on Electrical Engineering (FORTEI-ICEE), Bandung, Indonesia, 23–24 September 2020; pp. 80–85. [CrossRef]
8. Odo, P. Islanded dc Microgrid Design Using Non-Isolated Bidirectional Interleaved Half Bridge Converter for Energy Storage Application in a dc Microgrid. In Proceedings of the 2020 6th IEEE International Energy Conference (ENERGYCon), Gammarth, Tunisia, 28 September–1 October 2020; pp. 773–781. [CrossRef]
9. Gospodinova, D.; Milanov, K.; Georgiev, M.; Dineff, P. Battery Choice According to Weather Conditions of a Hybrid System Designed for a Single-Family House in Bulgaria. In Proceedings of the 2021 13th Electrical Engineering Faculty Conference (BulEF), Varna, Bulgaria, 8–11 September 2021; pp. 1–5. [CrossRef]
10. Moller, M.; Krauter, S. Model of an Automous PV Home using a Hybrid Storage System based on Li-ion batteries and Hydrogen Storage with Waste Heat Utilization. In Proceedings of the 2022 IEEE 49th Photovoltaics Specialists Conference (PVSC), Philadelphia, PA, USA, 5–10 June 2022; pp. 650–652. [CrossRef]
11. Datasheet: AccuForce 12V-100Ah Lead Acid Battery (VRLA). Available online: https://energypower.gr/wp-content/uploads/2017/04/accuforce-12v-100ah.pdf (accessed on 25 March 2023).
12. Alavi, S.M.M.; Mahdi, A.; Payne, S.J.; Howey, D.A. Identifiability of Generalized Randles Circuit Models. *IEEE Trans. Control Syst. Technol.* **2017**, *25*, 2112–2120. [CrossRef]
13. Sihvo, J.; Stroe, D.-I.; Messo, T.; Roinila, T. Fast Approach for Battery Impedance Identification Using Pseudo-Random Sequence Signals. *IEEE Trans. Power Electron.* **2019**, *35*, 2548–2557. [CrossRef]

14. Zhu, J.; Sun, Z.; Wei, X.; Dai, H. Studies on the medium-frequency impedance arc for Lithium-ion batteries considering various alternating current amplitudes. *J. Appl. Electrochem.* **2015**, *46*, 157–167. [CrossRef]
15. Wu, S.-L.; Chen, H.-C.; Chou, S.-R. Fast Estimation of State of Charge for Lithium-Ion Batteries. *Energies* **2014**, *7*, 3438–3452. [CrossRef]
16. Mohan, N.; Undeland, T.; Robbins, W. *Power Electronics, Converters, Applications and Design*, 3rd ed.; John Wiley & Sons: New York, NY, USA, 2003.
17. Zach, F. *Power Electronics, in German: Leistungselektronik*, 6th ed.; Springer: Frankfurt, Germany, 2022.
18. Rozanov, Y.; Ryvkin, S.; Chaplygin, E.; Voronin, P. *Power Electronics Basics*; CRC Press: Boca Raton, FL, USA, 2016.
19. Bosnjic, Z.; Krischan, K. Single-phase grid interface for home energy storage. *Elektrotech. Inftech.* **2023**, *140*, 103–109. [CrossRef]
20. Heydari-Doostabad, H.; Hosseini, S.H.; Ghazi, R.; O'Donnell, T. Pseudo DC-Link EV Home Charger With a High Semiconductor Device Utilization Factor. *IEEE Trans. Ind. Electron.* **2021**, *69*, 2459–2469. [CrossRef]
21. Kudryavtsev, A.; Zatsepina, V. Laboratory Installation to Demonstrate the Advantages of a DC Network in a Smart Home. In Proceedings of the 2022 2nd International Conference on Technology Enhanced Learning in Higher Education (TELE), Lipetsk, Russia, 26–27 May 2022; pp. 105–108. [CrossRef]
22. Carvalho, E.L.; Blinov, A.; Chub, A.; Vinnikov, D. Overview of Single-Stage Isolated AC-DC Topologies for Interfacing DC and AC Grids. In Proceedings of the 2022 IEEE 13th International Symposium on Power Electronics for Distributed Generation Systems (PEDG), Kiel, Germany, 26–29 June 2022; pp. 1–6. [CrossRef]
23. Carvalho, E.L.; Blinov, A.; Chub, A.; Vinnikov, D. Analysis of Holdup Time for DC Grid-Forming Isolated Active Front-End Converters. In Proceedings of the IECON 2022–48th Annual Conference of the IEEE Industrial Electronics Society, Brussels, Belgium, 17–20 October 2022; pp. 1–6. [CrossRef]
24. Sunny, A.C.; Surulivel, N.; Debnath, D. Solar-Battery-Integrated Hybrid AC/DC Off-Grid System for Rural Households Based on a Novel Multioutput Converter. *IEEE J. Emerg. Sel. Top. Power Electron.* **2022**, *10*, 6208–6217. [CrossRef]
25. Manas, K.; Gupta, J.; Singh, B. Roof Top Solar PV Supported Electric Vehicle Charging System for Home Parking Spaces. In Proceedings of the 2022 IEEE Industry Applications Society Annual Meeting (IAS), Detroit, MI, USA, 9–13 October 2022; pp. 1–6. [CrossRef]
26. Zhao, D.; Jiang, S.; Hu, D.; Wang, Y.; Jin, X.; Sun, C. Summary and Prospect of Technology Development of MVDC and LVDC Distribution Technology. In Proceedings of the 2022 IEEE 5th International Electrical and Energy Conference (CIEEC), Nangjing, China, 27–29 May 2022; pp. 1294–1300. [CrossRef]
27. Kaushik, H.; Bhushan, B. Performance Analysis of Boost Converters in a PV System with P and O based MPPT Controller connected to a Battery Backup and Grid. In Proceedings of the 2022 IEEE Delhi Section Conference (DELCON), New Delhi, India, 11–13 February 2022; pp. 1–7. [CrossRef]
28. Li, L.; Li, K.-J.; Sun, K.; Liu, Z.; Lee, W.-J. A Comparative Study on Voltage Level Standard for DC Residential Power Systems. *IEEE Trans. Ind. Appl.* **2022**, *58*, 1446–1455. [CrossRef]
29. Tyagi, S.; Singh, B. A Solar PV-Small Hydro Energy Conversion System Powered Charging Infrastructure. In Proceedings of the 2022 IEEE IAS Global Conference on Emerging Technologies (GlobConET), Arad, Romania, 20–22 May 2022; pp. 503–508. [CrossRef]
30. Himmelstoss, F.A. Design of State-Space Controllers with the Help of Signal Flow Graphs Shown for a Buck Converter. *WSEAS Trans. Syst.* **2022**, *21*, 421–429. [CrossRef]